Kelemen et al., **Ongoing alteration of mantle peridotite in the weathering horizon: Initial results from the Oman Drilling Project Multi-Borehole Observatory**

Supplementary Information

Supplementary Section 1: Results of thermodynamic calculations f or equilibria involving Oman fluids, serpentine and brucite.

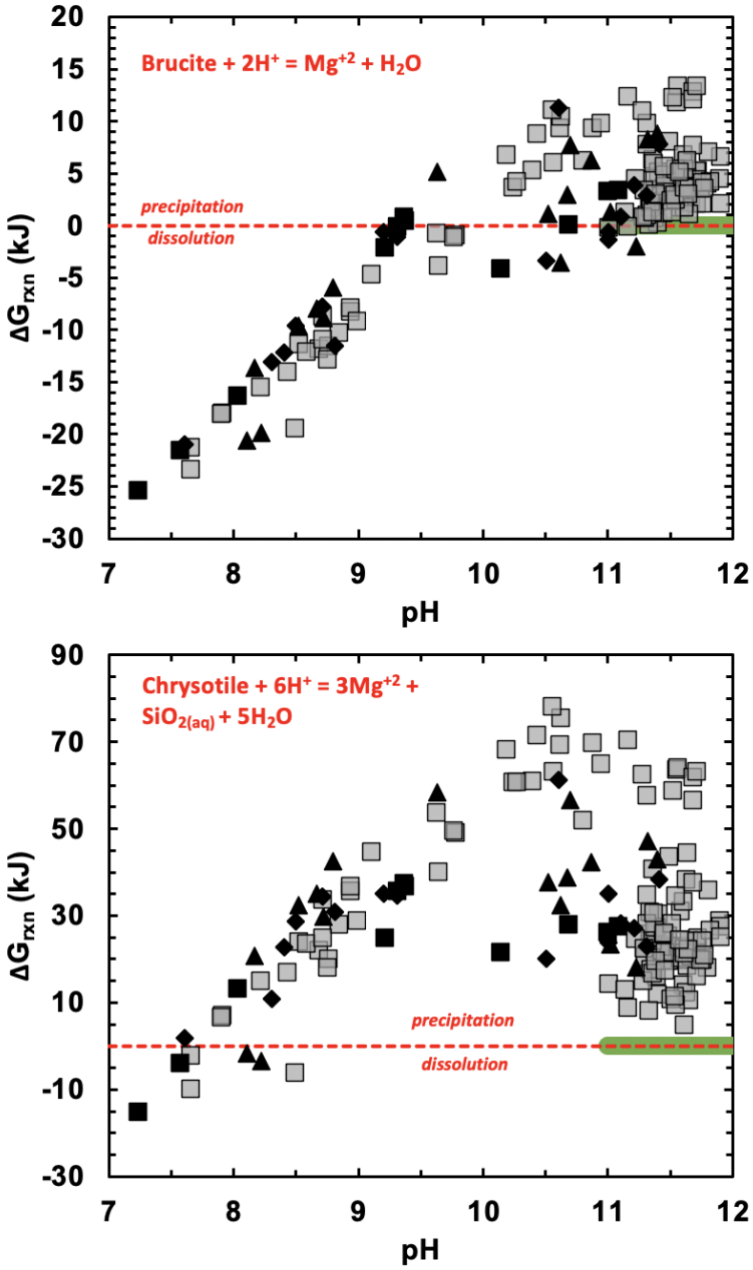

Methods used for these calculations, and general results, are described in the main text, Section 2.5.

***Supplementary Figure S1**: Extent of disequilibrium (in kilojoules per reaction) for the brucite (top panel) and chrysotile (bottom panel) dissolution reactions in various peridotite-hosted Samail ophiolite fluid compositions reported in previous studies. Horizontal green line depicts fluid with pH ranging from 11 to 12, at 40 °C, the pressure of sampling (1 bar for surface samples) and fO_2 at the H_2O-H_2 stability limit, in equilibrium with chrysotile and brucite. Surface fluids in grey squares: Paukert et al. ([Paukert et al., 2012]), Canovas et al. ([Canovas et al., 2017]), Leong et al. ([Leong et al., 2021]). Borehole fluids in black symbols: diamonds, Rempfert et al. ([Rempfert et al., 2017]); squares, Paukert Vankeuren et al. ([Paukert Vankeuren et al., 2019]); triangles, Nothaft et al. ([Nothaft et al., 2021a; Nothaft et al., 2021b]). Positive ΔG indicates that the fluid is saturated in brucite or chrysotile; negative values indicate that the fluid is undersaturated in brucite or chrysotile.*

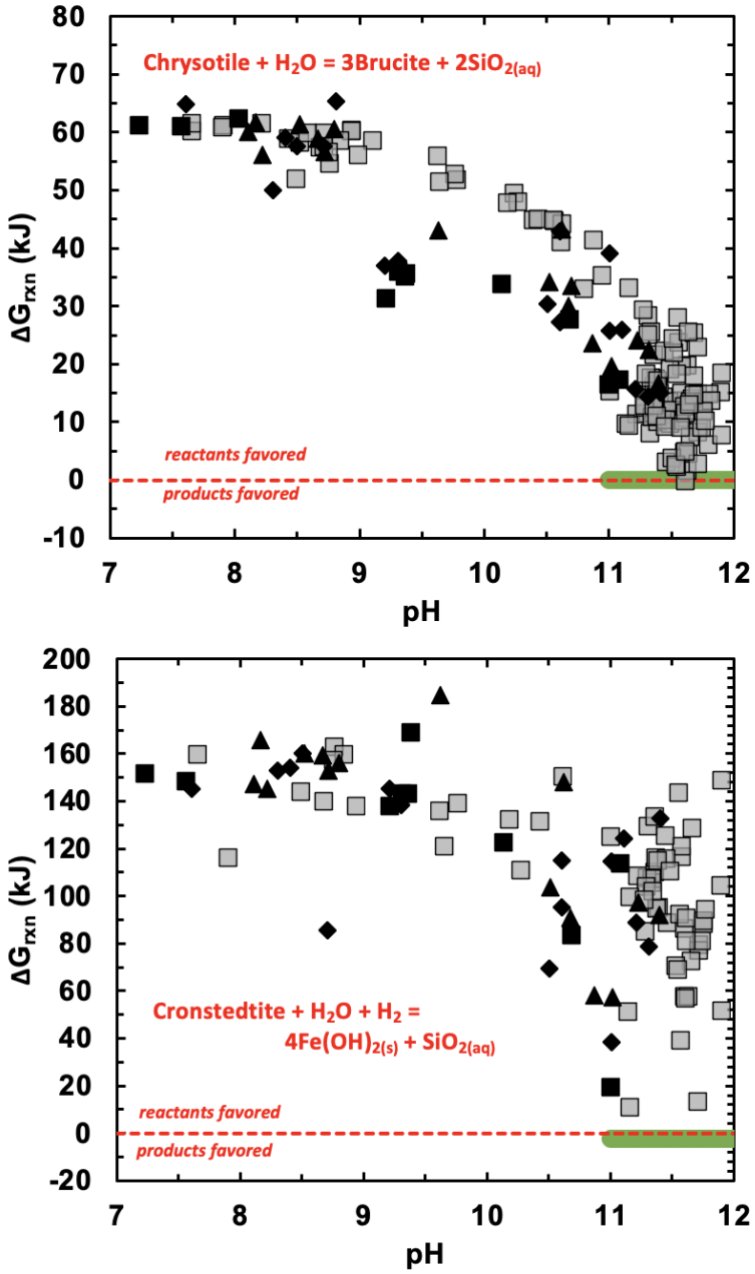

Supplementary Figure S2: Extent of disequilibrium (in kilojoules per reaction) provided by the serpentine breakdown or brucite silicification (top panel) and brucite oxidation or cronstedtite reduction (bottom panel) reactions in various peridotite-hosted Samail ophiolite fluid compositions reported in previous studies. Data sources and symbols as for Supplementary Figure S1. Positive ΔG indicates that SiO_2 in the fluid will react with brucite to form chrysotile or cronstedtite. Thus, brucite is metastable with respect to serpentine in all analyzed fluids from peridotite-hosted alkaline springs and boreholes in the Samail ophiolite.

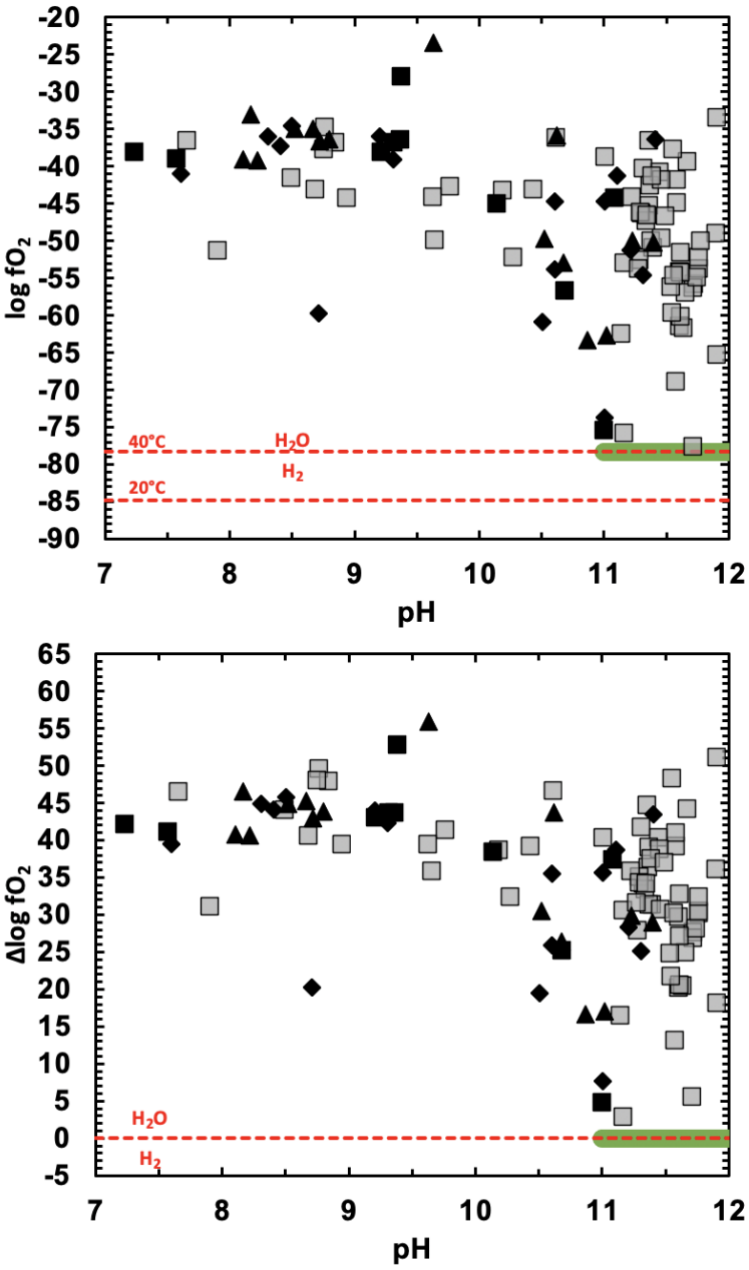

***Supplementary Figure S3**: Top panel: Oxygen fugacity (fO_2) calculated from measured Eh, pH and temperature of Oman fluids. Bottom panel: Difference in fO_2 from the calculated values in the top panel relative to the H_2O-H_2 limit at 40°C and 1 bar. Data sources and symbols as for Supplementary Figure S1. Based on these estimates, all analyzed fluids from peridotite-hosted alkaline springs and boreholes in the Samail ophiolite are undersaturated in H_2 gas. Indeed, this is consistent with measured dissolved H_2 contents in gas tight borehole samples to date (Hoelher, pers. comm. 2021). However, it is also apparent that some fluid compositions closely approach the H_2O-H_2 limit (on a log scale!), again consistent with some borehole sample data.*

Supplementary Section 2: Concentration of dissolved H_2 in borehole water samples compared to the sum of concentrations of other redox-sensitive solutes

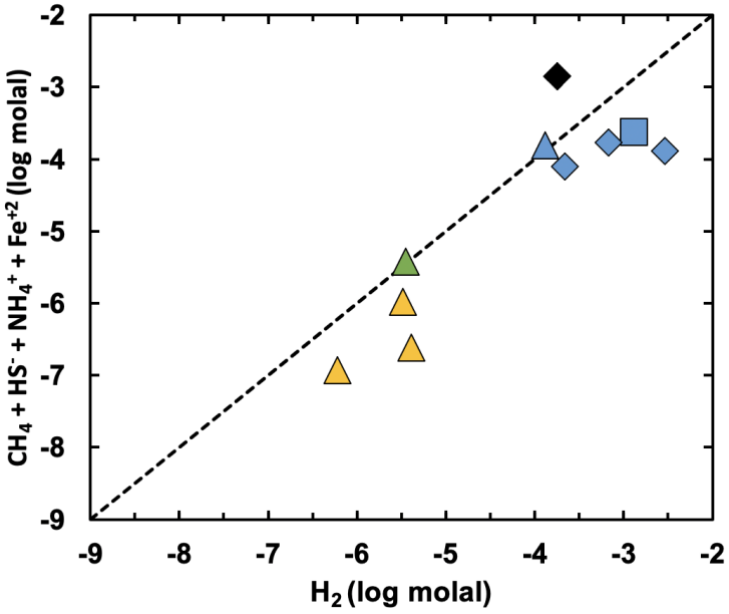

Supplementary Figure S4: *Concentration of dissolved H_2 vs the sum of concentrations of all other redox sensitive, dissolved species (CH4, HS-, NH4+, Fe+2) measured in discrete samples recovered from >50 m depth in MBO boreholes. Yellow, green, blue, and black symbols correspond to samples from BA1A, BA1D, NSHQ14 (nearby BA3A), and NSHQ04, respectively. Triangle, diamond, and square symbol represent data from Nothaft et al. [2021a; 2021b], Rempfert et al. [2017], and Paukert Vankeuren and co-workers [Paukert et al., 2012; Paukert Vankeuren et al., 2019], respectively.*

Supplementary Section 3: Propagation of uncertainty for estimates of fO_2 based on measurements of Eh, pH and temperature

Methods for calculating fO_2 from measurements of Eh, pH and temperature are described in Section 2.6, with results described in the text and illustrated in Figures 24, 28 and 30, as well as Supplementary Figure S3. We developed formalism for propagation of uncertainty for these calculated fO_2 values, which is presented here.

The formal uncertainty of $\log(fO_2)$ and $\log(fO_{2(limit)})$ in equations 5 and 6 in the main text can be calculated by assuming that the uncertainty in the measured E_h (σ_{Eh}) was 10 mV, the uncertainty in pH (σ_{pH}) was 0.1, the uncertainty in temperature (σ_T) was 0.05 K, and the uncertainty in pressure (σ_P) was 5 bars. These were determined by multiplying the manufacturer specifications for uncertainty of the instruments ***by a factor of 10*** for a conservative estimate of the real uncertainty in the field. These errors were propagated through the calculations above by taking the partial derivative with respect to Eh, pH, T, and P, multiplying by the corresponding uncertainty, and adding in quadrature, i.e.:

$$\sigma_{\log(fO_2)} = \sqrt{\left(\frac{\partial \log(fO_2)}{\partial E_h}\right)^2 \sigma_{Eh}^2 + \left(\frac{\partial \log(fO_2)}{\partial T}\right)^2 \sigma_T^2 + \left(\frac{\partial \log(fO_2)}{\partial pH}\right)^2 \sigma_{pH}^2}$$

$$\sigma_{\log(fO_{2(limit)})} = \sqrt{\left(\frac{\partial \log(fO_{2\_limit})}{\partial T}\right)^2 \sigma_T^2 + \left(\frac{\partial \log(fO_{2(limit)})}{\partial P}\right)^2 \sigma_P^2}$$

Which reduces to:

$$\sigma_{\log(fO_2)} = \sqrt{\left(\frac{20159.1}{T}\right)^2 \sigma_{Eh}^2 + \left(\frac{19174 - 20159.1 E_{measured}}{T^2}\right)^2 \sigma_T^2 + 16\sigma_{pH}^2}$$

$$\sigma_{\log(fO_{2(limit)})} = \sqrt{\left(\frac{29433.8}{T^2}\right)^2 \sigma_T^2 + \left(\frac{-2}{\ln(10)P}\right)^2 \sigma_P^2}$$

Finally, the uncertainty in $\Delta\log(fO2) = \log(\mathrm{fO_2}) - \log(\mathrm{fO_{2(limit)}})$ is:

$$\sigma_{\Delta\log(fO_2)} = \sqrt{\sigma^2_{\log(fO_2)} + \sigma^2_{\log(fO_{2(limit)})}}$$

Again, we assumed that actual measurement errors in field conditions were ***about*** ten times larger than the formal uncertainties arising from formal propagation of the manufacturer-provided uncertainties in measurements. As a result, hese calculations yield estimates of uncertainty that are ≤ ± 1 log unit of (fO_2) in bars. Also, as noted in Section 2.6, the fO_2 values calculated from Eh, pH and temperature measurements should be regarded as approximate because the fluids may contain multiple, redox sensitive solutes that are not in mutual equilibrium. Thus, there are several qualitative elements contributing to the actual uncertainty of the fO_2 estimates. As a result, we have not tabulated or illustrated the specific uncertainties for each fO_2 value. Instead, we infer and illustrate uncertainty bounds of ± 1 log unit of fO2 in Figure 30.

Supplementary Section 4: Sulfur concentration vs depth in Hole BA4A

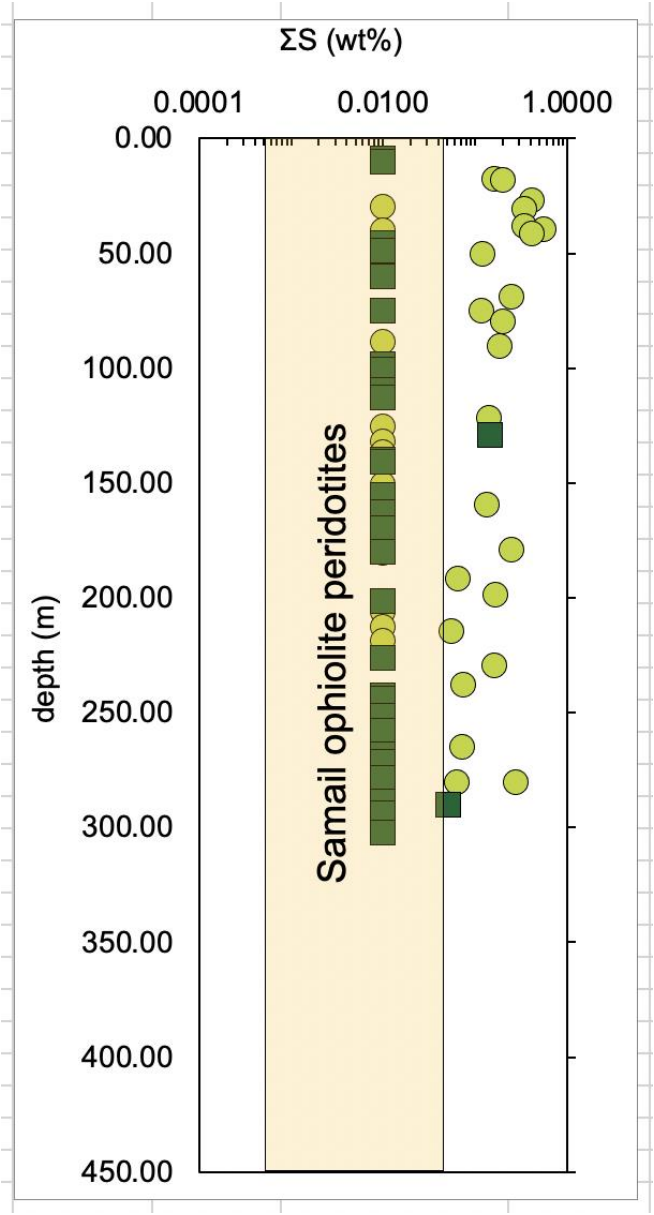

Figure S5: *Sulfur concentration versus depth in core from Hole BA4A [Kelemen et al., 2021]. Sulfur concentrations below the detection limit of shipboard analyses were assigned a value of 0.01 wt% (100 ppm). Orange bar illustrates previously measured range of sulfur concentration in mantle harzburgites and dunites in the Samail ophiolite, from 5 to 500 ppm [Hanghøj et al., 2010; Oeser et al., 2012]. Dunites: light green circles; harzburgites: dark green squares.*

Supplementary Section 5: Evaluation of the hypothesis that addition of igneous minerals to residual mantle harzburgites produced low Mg/Si at a given Al/Si in core samples from the MBO

As shown in Figure 26 and discussed in Section 4.3 in the main body of the paper, core samples of harzburgite from Holes BA1B, BA3A and BA4A have low wt% MgO/SiO_2 at a given wt% Al_2O_3/SiO_2 (hereafter, Mg/Si and Al/Si for brevity) compared to the residues of partial melting and melt extraction from the mantle. The discussion in the main text mentions three possible reasons for low Mg/Si at a given Al/Si in these samples: (1) Mg dissolution and removal from the rocks (2) Si addition, and (3) igneous "impregnation", for example by crystallization of small amounts of relatively Al-rich, Si-rich, Mg-free plagioclase feldspar in pore space in residual peridotites in the shallow mantle. This section of the Supplementary Information evaluates, and rejects, the third of these hypotheses. We do this primarily graphically, with a minimum of explanatory text.

The terms "impregnated peridotite", "impregnated dunite", and sometimes (usually, erroneously) "troctolite" are used to refer to rock with added, igneous minerals precipitated during migration of melt through pre-existing, residual mantle peridotites and dunite conduits, as outlined in Sections 1.2 and 4.1 of the main text. 100% crystallization of added melt would produce a geochemical trend more or less identical to the melt extraction trend illustrated by the red symbols in Figure 26. However, commonly the minerals added to impregnated peridotites are "cumulate", in the sense that they are precipitated by partial crystallization of a melt, after which the remaining melt is removed from the rock. In various cases, the presence of individual minerals (typically, calcium-rich pyroxene, cpx, and/or plagioclase, but in some cases Ca-poor pyroxene, opx), or mixtures of these minerals, are attributed to impregnation.

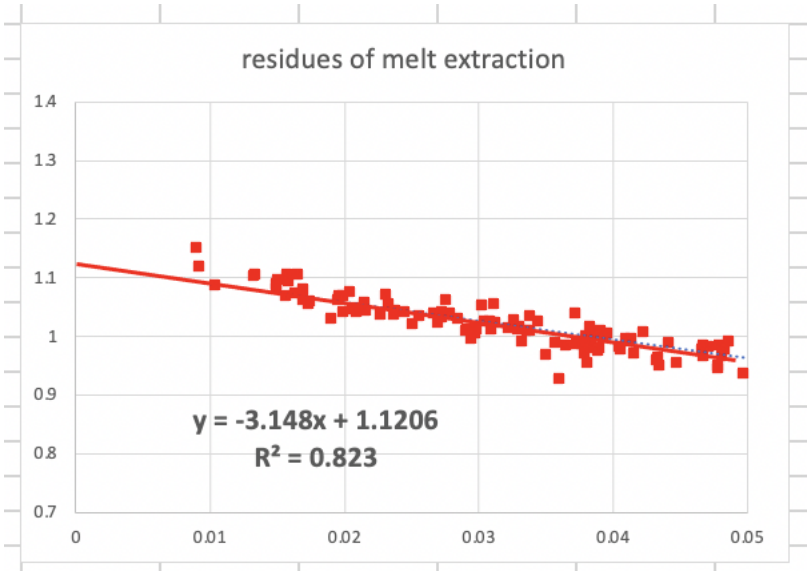

***Figure S6**: For reference the residues of melt extraction from Figure 26 are plotted again here.*

As an end-member residual peridotite, we use a harzburgite with 10 wt% opx, 90 wt% olivine, a molar Mg# (molar Mg/(Mg+Fe)) of 0.9, and Al/Si of 0.005 (perhaps with Al in spinel), ~ 42.6 wt% SiO_2, 0.2 wt% Al_2O_3, 9.0 wt% FeO and 48.2 wt% MgO.

The mineral plagioclase is a solid solution primarily composed of end-members anorthite ($CaAl_2Si_2O_8$) and albite ($NaAlSi_3O_8$). Neither addition of 4 wt% anorthite, nor addition of 4 wt% albite, reproduces the compositions of MBO harzburgites illustrated in Figure 26.

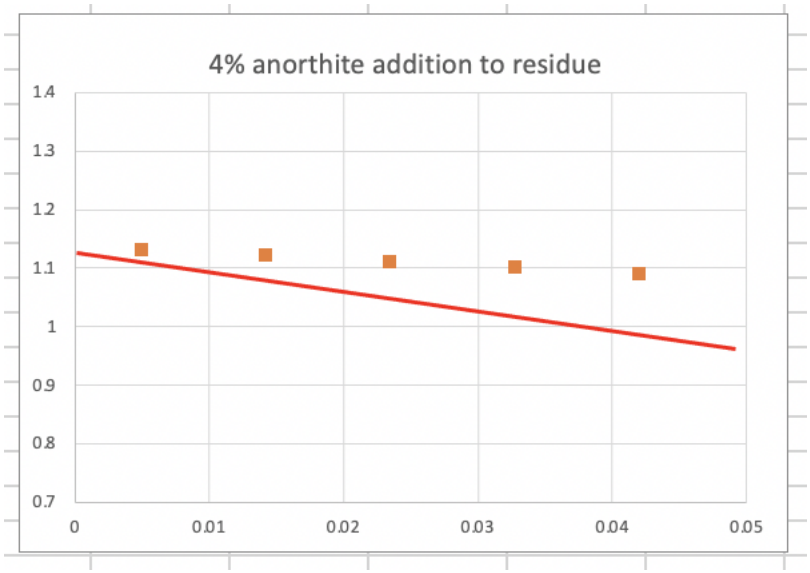

Figure S7

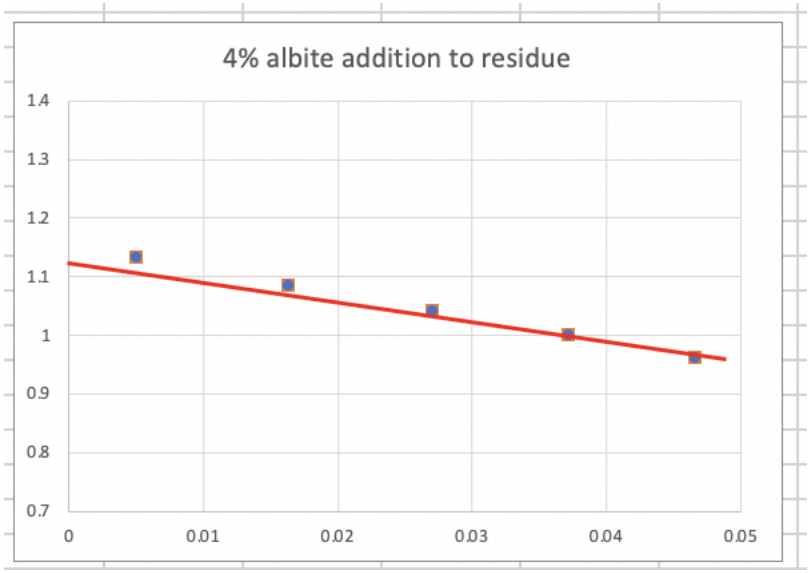

Figure S8

There are many sources of data on mineral compositions in peridotites from the Samail ophiolite. For brevity and simplicity, here we simply use averages from the extensive data of Monnier et al. [2006]. Neither 10 wt% addition of cpx, nor 10 wt% addition of opx, reproduces the compositions of MBO harzburgites illustrated in Figure 26. Addition of more than 10 wt% either pyroxene would produce CaO and/or SiO2 concentrations much higher than in most MBO harzburgites, and optically evident, high pyroxene abundances that are not observed in MBO core.

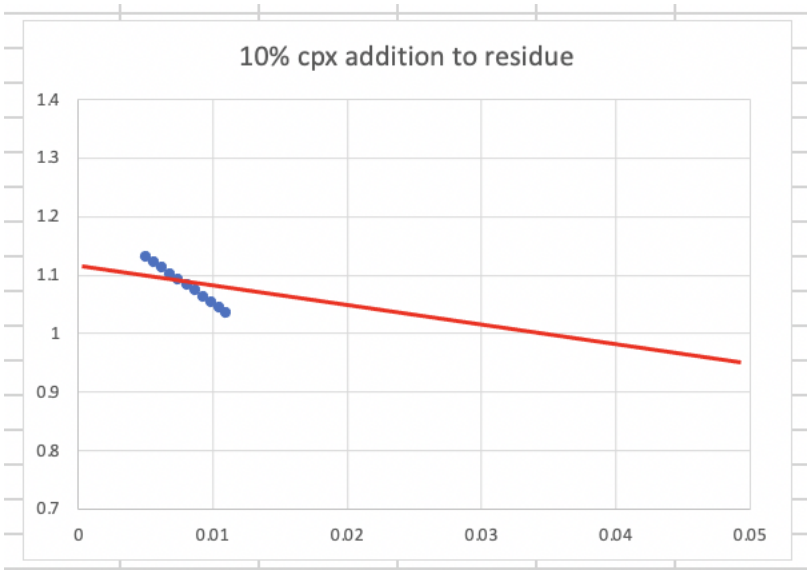

Figure S9

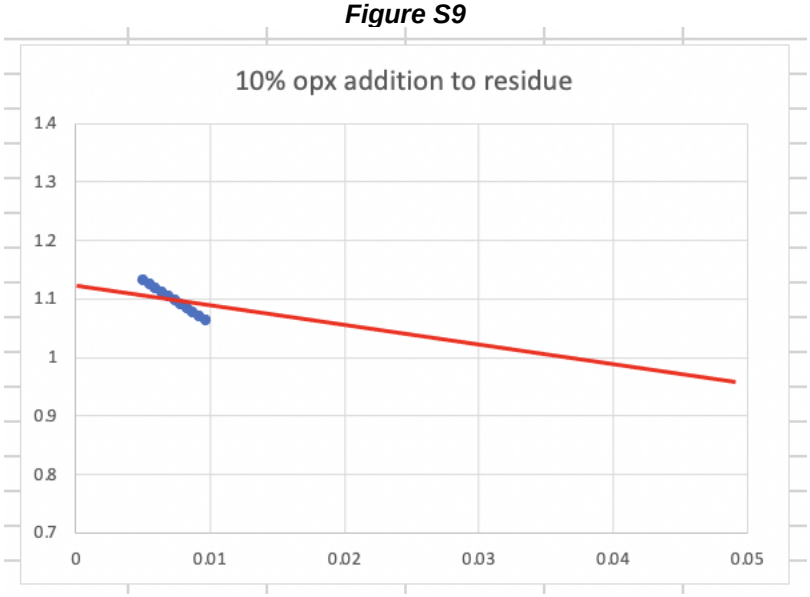

Figure S10

We also tested various mixtures of minerals, which also failed to reproduce the compositions of MBO harzburgites illustrated in Figure 26.

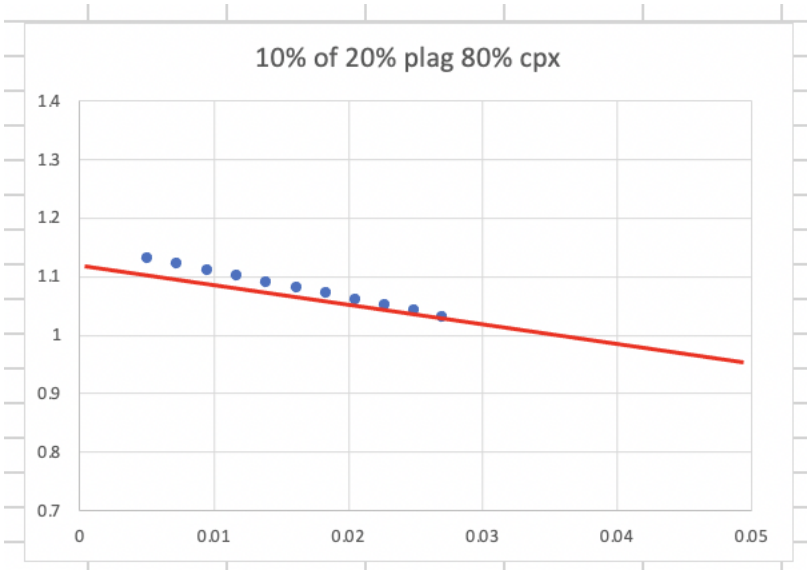

Figure S11

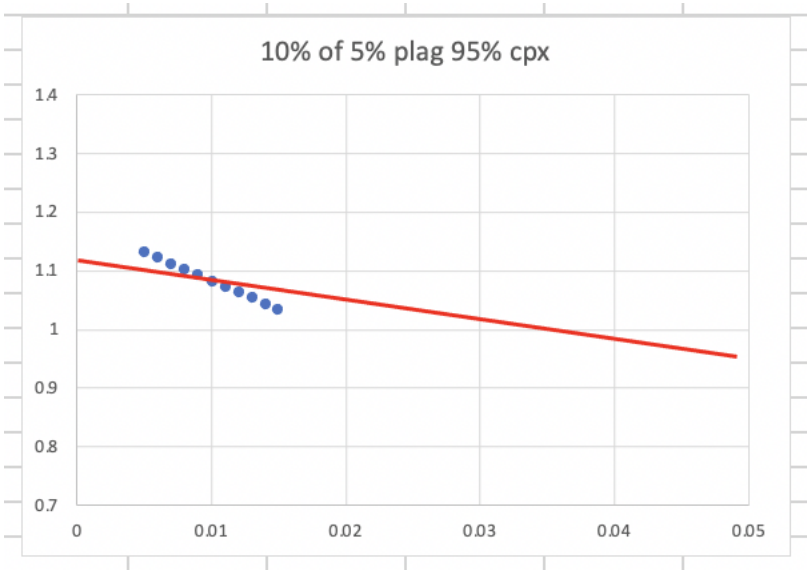

Figure S12

As a result of these and several other, related calculations, we conclude that igneous impregnation cannot explain the low Mg/Si at a given Al/Si observed in MBO harzburgites (Figure 26).

Supplementary Section 6: Plots of Mg/Si deficit vs Mg# and depth

As noted in Section 4.3 of the main text, if the observed low Mg/Si in MBO harzburgites were due to Mg extraction, one would expect to see a correlation between the Mg/Si deficit (equation 9) and Mg# (molar Mg/(Mg+Fe)). In Figure S12, we show that such correlations are not observed, and futher that there is no correlation between the Mg/Si defict with depth in the cored MBO Holes.

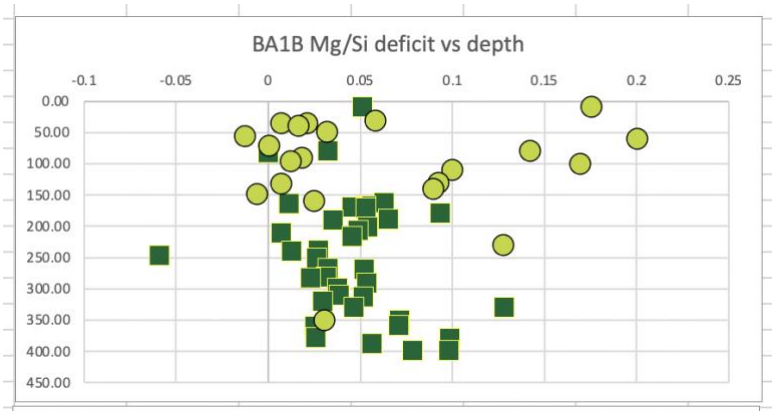
BA1B Mg/Si deficit vs depth
-0.1
-0.05
0
0.05
0.1
0.15
0.2
0.25
0.00
50.00
100.00
150.00
200.00
250.00
300.00
350.00
400.00
450.00

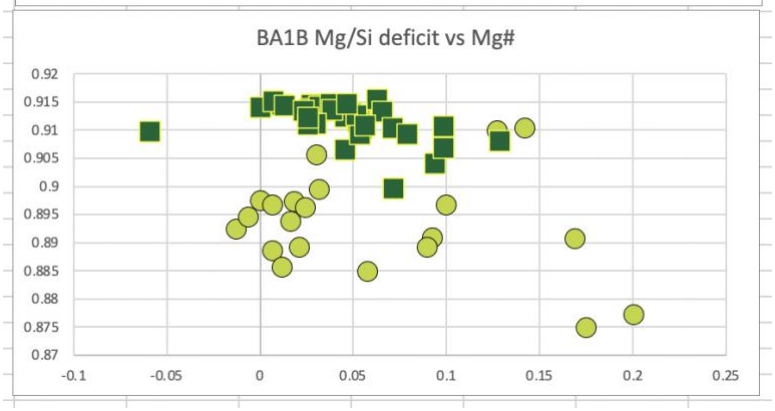
BA1B Mg/Si deficit vs Mg#
0.92
0.915
0.91
0.905
0.9
0.895
0.89
0.885
0.88
0.875
0.87
-0.1
-0.05
0
0.05
0.1
0.15
0.2
0.25

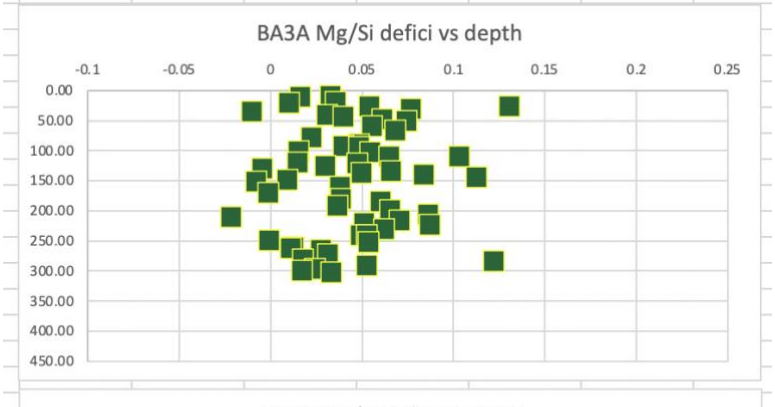
BA3A Mg/Si defici vs depth
-0.1
-0.05
0
0.05
0.1
0.15
0.2
0.25
0.00
50.00
100.00
150.00
200.00
250.00
300.00
350.00
400.00
450.00

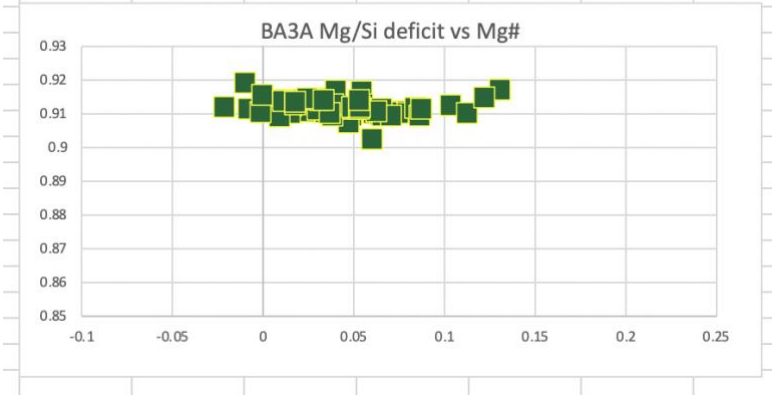
BA3A Mg/Si deficit vs Mg#
0.93
0.92
0.91
0.9
0.89
0.88
0.87
0.86
0.85
-0.1
-0.05
0
0.05
0.1
0.15
0.2
0.25

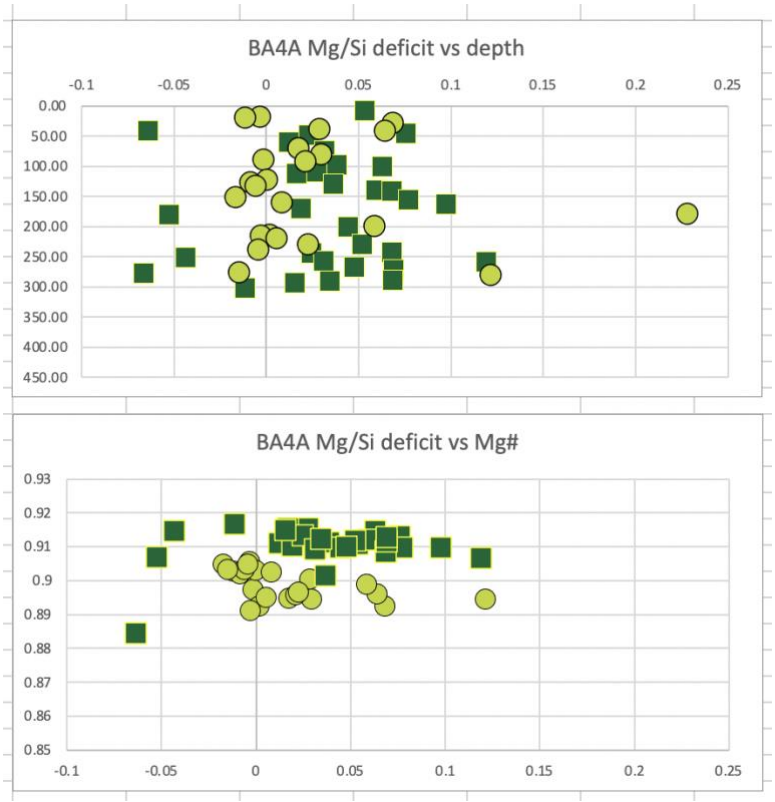

Figure S14: *Plots of Mg/Si deficit vs Mg# and depth for the three cored MBO Holes.*

Supplementary Section 6: Additional results of reaction-path modeling

Figure 29 in the main text presents results of reaction path modeling at 35°C and 50 MPa. The righthand panels in that figure illustrate results from Step 2 of the modeling, involving reaction of Type 1, Mg-HCO3 rich waters with peridotite, isolated from the atmosphere, as described in Sections 2.5 and 4.6. Here, in Figure S13, we provide a few more results from Step 2. We invite readers to look at the caption for Figure 29 to aid in understanding Figure S13.

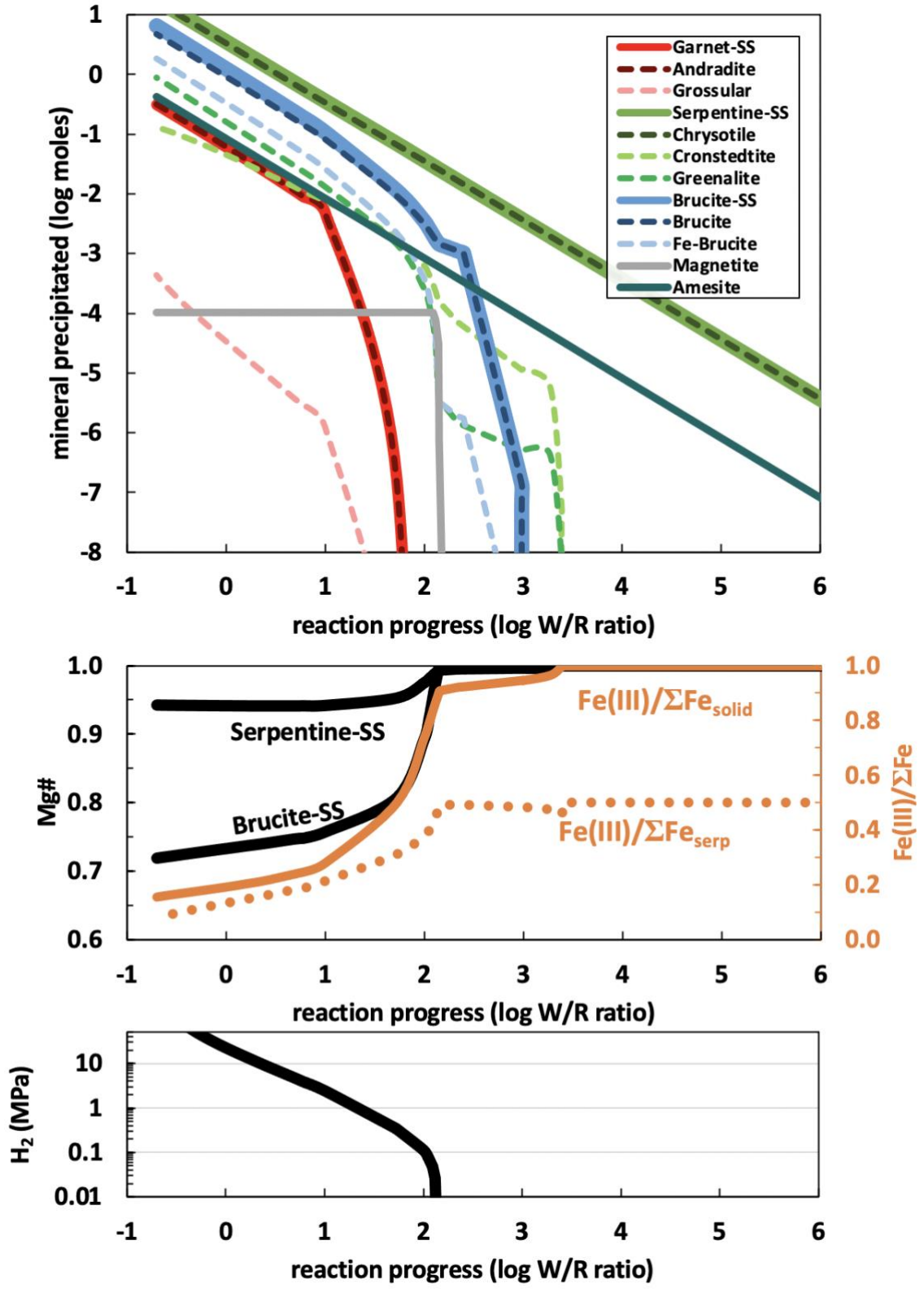

***Figure S13**: Additional results from reaction path modeling at 35°C and 50 MPa, as described in Sections 2.5 and 4.6, and presented in Figure 29. Here we provide some details of phase proportions and compositions, as well as the calculated partial pressure of dissolved H_2 produced in the model. In addition to results described in the text and the caption for Figure 29, the main point to take from this figure is information about the composition of precipitating brucite and serpentine solid solutions. Initially, at water/rock ratios greater than 100, precipitating serpentine is composed almost entirely of $(Mg,Fe^{2+})_2Fe^{3+}SiFe^{3+}O_5(OH)_2$ - Mg-Fe^{2+}-cronstedtite, with molar $Mg/(Mg+Fe^{2+})$, or Mg#, close to 1. With increasing reaction progress, at water/rock ratios less than 100, brucite begins to crystallize, with increasingly large proportions of Fe^{2+} (lower Mg#) and no Fe^{3+}, while the serpentine solid solution contains increasingly large amounts of greenalite and chrysotile components. Both of these factors lead to increasingly low Fe^{3+}/(Fe total) in the crystallizing phase assemblage. Thus, Fe^{3+}/(total Fe) in the serpentine solid solution drops by a factor of about 5, and Fe^{3+}/(total Fe) in the total crystallizing assemblage drops by a factor of ~ 10. However, meanwhile, the mass of crystallized serpentine + brucite increases by more than a factor of 100 during reaction progress from water/rock ratio of ~ 100 to $10^{-0.8}$. As a result, as shown in Figure 29, the total amount of Fe^{2+} that is oxidized to form Fe^{3+} continues to increase throughout the reaction path, together with decreasing fO_2 and an increasing partial pressure of H_2.*

To reiterate, (déjà vu all over again!) the reaction path modeling was done at a pressure 50 MPa, whereas the maximum pressure at the bottom of MBO boreholes is ~ 4 MPa. At 4 MPa and 35°C, the partial pressure of H_2 would not increase above 4 MPa, fO_2 would be limited to a maximum value of ~ 10^{-83}, but oxidation of Fe^{2+} to Fe^{3+} would proceed, together with formation of H_2 gas.

Supplementary Section 7: References cited in this supplement

Canovas, P. A., T. Hoehler, and E. L. Shock (2017), Geochemical bioenergetics during low-temperature serpentinization: An example from the Samail ophiolite, Sultanate of Oman, *J. Geophys. Res. Biogeosci,. 122*, 1821–1847.

Hanghøj, K., P. Kelemen, D. Hassler, and M. Godard (2010), Composition and genesis of depleted mantle peridotites from the Wadi Tayin massif, Oman ophiolite; Major and trace element geochemistry, and Os isotope and PGE systematics, *Journal of Petrology*, *51*, 201-227.

Kelemen, P. B., J. M. Matter, D. A. H. Teagle, J. A. Coggon, and Oman Drilling Project Science Team (2021), Site BA4, in *Proceedings of the Oman Drilling Project*, edited by P. B. Kelemen, J. M. Matter, D. A. H. Teagle, J. A. Coggon and et al., pp. 1-97, International Ocean Discovery Program, College Station, TX.

Leong, J. A. M., A. E. Howells, K. J. Robinson, A. Cox, R. V. Debes II, K. Fecteau, P. Prapaipong, and E. L. Shock (2021), Theoretical predictions vs environmental observations on serpentinization fluids: Lessons from the Samail ophiolite in Oman, *J. Geophys. Res.*, *126*, e2020JB020756.

Monnier, C., J. Girardeau, L. Le Mée, and P. M. (2006), Along-ridge petrological segmentation of the mantle in the Oman ophiolite, *G-cubed*, *7*, doi:10.1029/2006GC001320.

Nothaft, D. B., A. S. Templeton, E. S. Boyd, J. M. Matter, M. Stute, A. N. Paukert Vankeuren, and O. D. P. S. Team (2021a), Aqueous geochemical and microbial variation across discrete depth intervals in a peridotite aquifer assessed using a packer system in the Samail Ophiolite, Oman, *J. Geophys. Res.*, *in review*, preprint available at https://www.essoar.org/doi/abs/10.1002/essoar.10506402.10506402

Nothaft, D. B., et al. (2021b), Geochemical, biological and clumped isotopologue evidence for substantial microbial methane production under carbon limitation in serpentinites of the Samail Ophiolite, Oman, *J. Geophys. Res.*, *in review*, preprint available at https://www.essoar.org/doi/abs/10.1002/essoar.10504124.10504121.

Oeser, M., H. Strauss, P. E. Wolff, J. Koepke, M. Peters, D. Garbe-Schönberg, and M. Dietrich (2012), A profile of multiple sulfur isotopes through the Oman ophiolite, *Chem. Geol.*, *312-313*, 27-46.

Paukert, A. N., J. M. Matter, P. B. Kelemen, E. L. Shock, and J. R. Havig (2012), Reaction path modeling of enhanced in situ CO2 mineralization for carbon sequestration in the peridotite of the Samail Ophiolite, Sultanate of Oman, *Chem. Geol.*, *330-331*, 86-100.

Paukert Vankeuren, A. N., J. M. Matter, M. Stute, and P. B. Kelemen (2019), Multitracer determination of apparent groundwater ages in peridotite aquifers within the Samail Ophiolite, Sultanate of Oman, *Earth Planet Sci. Lett.*, *516*, 37-48.

Rempfert, K. R., H. M. Miller, N. Bompard, D. Nothaft, J. M. Matter, P. Kelemen, N. Fierer, and A. S. Templeton (2017), Geological and geochemical controls on subsurface microbial life in the Samail Ophiolite, Oman, *Frontiers in Microbiology*, Article 56.